Thermo-Structural Modelling of a Plasma Discharge Tube for Electric Propulsion

D. de Faoite[a], D. J. Browne[a], J. I. Del Valle Gamboa[b], K. T. Stanton[a,*]

[a] *UCD School of Mechanical and Materials Engineering, University College Dublin, Ireland*
[b] *Ad Astra Rocket Company, Liberia, Costa Rica*

Abstract

Potential thermal management strategies for the plasma generation section of a VASIMR® high-power electric propulsion space thruster are assessed. The plasma is generated in a discharge tube using helicon waves. The plasma generation process causes a significant thermal load on the plasma discharge tube and on neighbouring components, caused by cross-field particle diffusion and UV radiation. Four potential cooling system design strategies are assessed to deal with this thermal load. Four polycrystalline ceramics are evaluated for use as the plasma discharge tube material: alumina, aluminium nitride, beryllia, and silicon nitride. A finite element analysis (FEA) method was used to model the steady-state temperature and stress fields resulting from the plasma heat flux. Of the four materials assessed aluminium nitride would result in the lowest plasma discharge tube temperatures and stresses. It was found that a design consisting of a monolithic ceramic plasma containment tube fabricated from aluminium nitride would be capable of operating up to a power level of at least 250 kW.

Keywords: thermo-structural modelling, plasma, discharge tube, electric propulsion

*Corresponding author
Email address: kenneth.stanton@ucd.ie (K. T. Stanton)

1. Introduction

The Variable Specific-Impulse Magnetoplasma Rocket [1, 2, 3, 4] (VASIMR®) is an electric propulsion space thruster being developed by the Ad Astra Rocket Company (Houston, Texas, U.S.A). It uses a magnetically-confined plasma for high-specific impulse propulsive thrust. The plasma is ionised using helicon electromagnetic waves [5, 6] in what is thereby known as the helicon section of the engine. Following ionisation, the plasma is heated by electromagnetic waves at the ion cyclotron resonance frequency, termed ion cyclotron resonance heating (ICRH), significantly increasing the ion temperature [7, 8]. A magnetic nozzle converts the azimuthal kinetic energy of the ions into axial kinetic energy and facilitates detachment of the plasma from the magnetic field [9]. VASIMR® has no electrodes or grid in contact with the plasma, allowing heating of the plasma to very high temperatures and allowing long operational lifetime. The high energy plasma results in VASIMR® having a high designed specific impulse [10]. Electrical power for VASIMR® may be supplied by stored-battery, solar, radio-isotope thermal generator, or a suitable nuclear reactor [11].

A VASIMR® device with 200 kW of RF power is being developed by the Ad Astra Rocket Company [12, 13]. Representative operating parameters for the VASIMR® VX-200 are shown in Table 1.

1.1. VASIMR® Hardware Configuration

A schematic representation of the hardware configuration of VASIMR® is shown in Figure 1. A plasma discharge tube, otherwise known as a gas containment tube (GCT) is used in the helicon section to contain the neutral gas prior to ionisation and to ensure physical separation between the neutral gas and the helicon antenna. Gaseous propellant, typically argon or krypton, is injected through a metal endplate into the GCT. An RF antenna called the helicon antenna encircles the GCT. The plasma is created under the helicon antenna and flows downstream (from left to right in Figure 1) from the GCT through a 'choke'—a tapered component that aids in the ionisation of the plasma. The

Table 1: Representative operating parameters for the VASIMR® VX-200.

Quantity	Value
DC power input	211 kW
Total RF power	200 kW
RF power to ICRH section	165 kW
RF power to helicon section	35 kW
Propellant	Argon
Propellant flowrate	$150\,\mathrm{mg \cdot s^{-1}}$
Thrust	6.7 N
Exhaust velocity	$50\,\mathrm{km \cdot s^{-1}}$

helicon antenna is located in a cylindrical high-vacuum enclosure, and has a quarter-turn left-hand helical design. The helicon antenna causes ionisation of the netural gas to create the plasma, while an ICRH antenna farther downstream significantly increases the plasma temperature.

The helicon hardware components (GCT, endplate, choke and antenna) are key to the operation of the device. They comprise the plasma generation chamber, and form a first wall intercepting waste heat from the plasma. The endplate and choke provide a vacuum-tight seal between the plasma generation region and the high-vacuum surrounding region, required for correct operation of the helicon antenna. Additionally, the endplate and choke dissipate waste heat from the plasma. The endplate is supported at its upstream end by composite standoff rods, and the choke is connected at its downstream end to the ICRH hardware components.

Super-conducting electromagnets are located radially outside this cylindrical vacuum enclosure, encircling the endplate, GCT, antenna and choke. These magnets provide the magnetic field required to support the propagation of helicon waves and also to contain the plasma, once ionised. A magnet called the choke magnet is located at the downstream end of the choke, and further

Nomenclature

A	Albedo of the earth's surface
A_r	Radiator surface area
F	Normalised axial heat flux profile
$\bar{F}$	Averaged normalised axial heat flux profile
f_int	Emitted heat flux from onboard generated heat
f_IR	Absorbed heat flux from IR emission from the earth
f_ref	Absorbed heat flux from radiation reflected from the earth
f_sol	Absorbed heat flux from direct solar radiation
H	Orbital altitude
N_e	Number of experiments
P_RF	Applied RF power
q	Heat flux
q_p	Peak heat flux
Q_int	Rate of onboard heat generation
r	Radius
R_e	Radius of the earth
S	Solar constant (solar heat flux) at 1 astronomical unit
T_e	Temperature of the earth's surface
T_eq	Equilibrium temperature
z	Axial coordinate
α_r	Radiator panel absorptivity
ε_e	Emissivity of the earth
ε_r	Emissivity of the radiator surface
ζ	View factor
η	Fin effectiveness of the radiator panel
θ_p	Angle between plane of radiator and nadir
θ_s	Angle between plane of radiator panel and the sun
λ	Ratio of peak heat flux to applied RF power

Nomenclature (Continued)

λ	Ratio of peak heat flux to applied RF power
σ	Stefan-Boltzmann constant
σ_1	Maximum principal stress
σ_2	Middle principal stress
σ_3	Minimum principal stress
σ_c	Compressive strength
σ_f	Flexural strength
σ_t	Tensile strength
τ_e	Transmissivity of the earth's atmosphere

magnets are located in the ICRH section.

1.2. Thermal Management Requirement

The helicon plasma generation process is not completely efficient and results in a portion of the input RF energy being lost as waste heat. This heat is deposited on the inner surface of the endplate, GCT and choke by UV radiation and cross-field particle diffusion [15, 16]. To allow successful operation of the device, an adequate thermal management system is essential. Heat needs to be extracted from the gas containment tube and rejected to space using thermal radiators. For ground prototypes, heat is rejected to heat exchangers.

No electrically-conducting materials can be used in close proximity to the RF antenna to avoid coupling energy directly from the antenna. A design rule-of-thumb called the '$4x$' rule is used, that states: the radial separation of metallic components from the antenna must be at least 4 times the radial separation between the antenna and plasma. This minimum radial separation between the antenna and other metallic components is termed the $4x$-distance. In addition, metallic components should not be located axially within half an antenna width of the antenna. An electrically-insulating ceramic material must therefore be

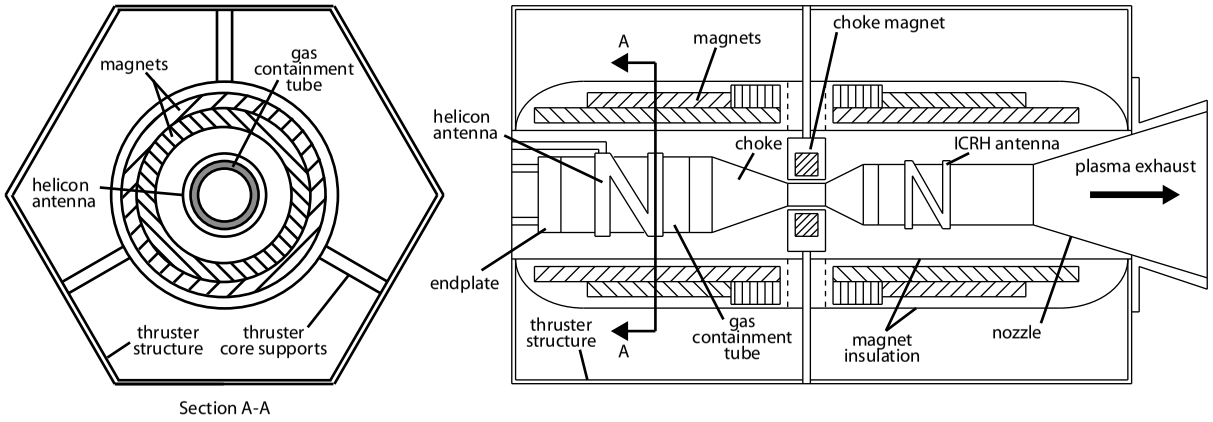

Figure 1: Schematic representation of VASIMR® hardware. Adapted from [14].

used for the GCT. To minimise dielectric heating of this component, the GCT material must have a low dielectric loss tangent. Due to the high elastic moduli of these ceramic materials [17], non-uniformities in the temperature fields in these components generate significant mechanical stresses. These stresses could lead to failure of these components if the strength of the material is exceeded. This directly impacts the lifetime of the helicon stage, and of the whole VASIMR® system.

Temperature field non-uniformities, and particularly "hot-spots" in the temperature field of the GCT, may occur at regions where the concentration of ion impingment into the inner surface of the GCT is high. These phenomena are caused by interactions of the plasma with its magnetic and electrical environment, and can cause continuous sputtering of the material at the point of ion impact. Therefore, a non-uniform thermal profile in the GCT is also associated with potential failure of the helicon source due to the erosion of the tube's inner surface.

The heat flow to the superconducting magnets must be minimised. For this reason, heat cannot be extracted radially outward through the vacuum wall, but must instead be extracted axially upstream. The location of the choke magnet and ICRH section downstream from the helicon section precludes the possibility for extracting heat in the downstream axial direction. The vacuum section wall acts as a thermal barrier between the high-temperature plasma-facing hardware and the magnets. Multi-layer insulation (MLI) is used to limit radiative heat transfer to the vacuum wall.

The goal of this work is to assess the effect of the plasma heat load on the operation of the VASIMR® device, and to develop a design to allow the continuous operation of the device up to RF power levels of 250 kW. Such designs would also be applicable to other high-power helicon plasma experiments and plasma-based electric propulsion devices. The scope of this paper is to present calculations of the expected heat loads, to present analyses of possible designs, and to confirm that the resultant system is capable of operating to input power levels of at least 250 kW.

1.3. Review of Thermal Management Strategies in Related Devices

The majority of laboratory helicon plasma sources operate at relatively low power levels of less than 2 kW (e.g. devices described in references [18, 19, 20]). For this class of device the standard materials to use for the plasma discharge tube are fused quartz or borosilicate glass [18, 19, 20, 6, 21, 22]. At these power levels a dedicated cooling system is typically not required for the plasma discharge tube, as the tube may radiate away sufficient heat without exceeding its maximum allowable operation temperature [23]. Primarily for this reason little exists in the open literature about the design of cooling strategies for helicon plasma generation devices. In contrast, the power input of the presently considered VASIMR® device is significantly higher, requiring the use of a dedicated cooling system.

Sedwick & DeMaio proposed a thermal management system design for a helicon thruster intended to operate at 8 kW of electrical power input [24]. Their design consisted of a fused quartz plasma discharge tube encircled by a layer of copper to intercept radiant heat from the plasma, and conduct it downstream to where it would be radiated away. Two concentric ceramic layers would be located radially outside the copper layer, separated from each other by a vacuum gap in order to minimise heat transfer to the device's superconducting electromagnets. This cooling system would not be practical for the presently-considered VASIMR® device, primarily because a copper layer covering the outer surface of the plasma discharge tube would interfere with the coupling of helicon waves from the antenna to the plasma.

2. Cooling System Design Options

Four main different classes of heat extraction solution have been identified for the helicon section: axial conductive cooling of the GCT, convective cooling of the GCT, radiative cooling of the GCT, and radial conductive cooling of the GCT.

2.1. Axial Cooling

The strategy of axial cooling is to attempt to dissipate the waste heat deposited on the inside surface of the GCT by passively or actively cooling the endplate and choke to low temperature and conducting the heat axially from the GCT. In previous VASIMR® prototypes the endplate, choke, and antenna have been convectively water-cooled, while the GCT was not directly cooled. Instead, heat was dissipated from the GCT by axial conduction into the endplate and choke. The axial cooling concept is illustrated schematically in Figure 2a.

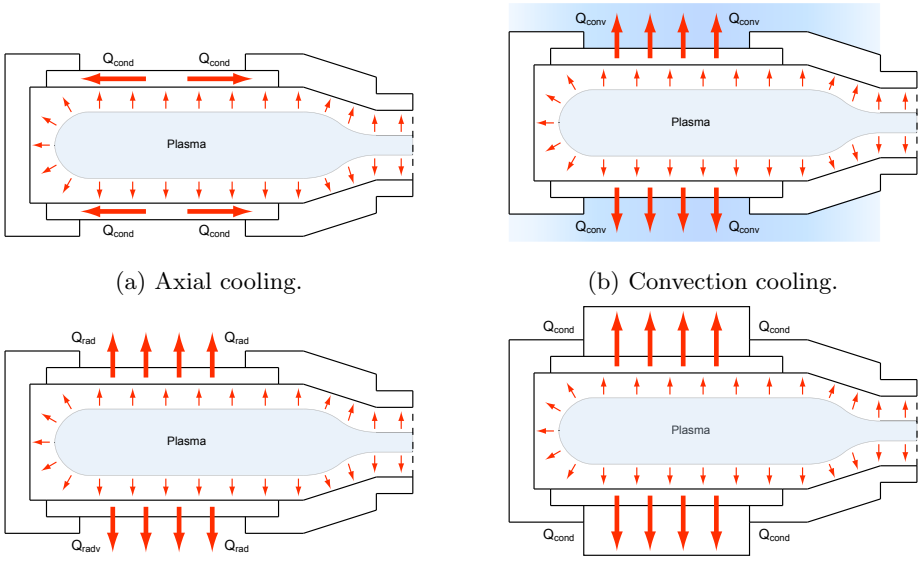

(a) Axial cooling.

(b) Convection cooling.

(c) Radiative cooling.

(d) Radial cooling.

Figure 2: Cooling system conceptual designs.

This design is adequate for low to medium power ground prototypes. Indeed, this cooling strategy has been successfully used in previous low-power VASIMR® prototypes. However, the design is fundamentally limited in its power-handling capabilities by the thermal transport properties of the GCT material. With a low thermal conductivity material, this design can lead to large temperature gradients in the GCT, causing high or excessive thermal stresses and temperatures. The GCT thickness may be, to a limited extent, increased

in order to reduce the axial temperature gradients, by creating a greater cross-sectional area for axial heat flow.

The axial cooling strategy results in a relatively low-mass design. However, this strategy may result in high temperatures, due to the high temperature gradients required to drive the heat flow.

2.2. Fluid-Assisted Active Cooling

For higher powered VASIMR® prototypes active fluid-based cooling strategies may be required. One attraction of pumped fluid based cooling is that it offers the capacity for very high rates of heat removal. The convection cooling concept is illustrated schematically in Figure 2b. The fluid used for such designs should have high thermal conductivity, low viscosity, and high critical point temperature. The fluid would also need to be a dielectric and have a low dissipation factor. Many different configurations of convective cooling of the GCT are possible, including convective cooling of an annular gap between two concentric dielectric tubes in place of a single GCT, or flood cooling of the space surrounding the GCT. One major advantage of fluid-assisted active cooling is that due to the lower temperatures, there may be lower thermal stresses and CTE mismatch at seals and interfaces.

2.3. Radiative Cooling

The goal of the radiation cooling strategy is to reject the waste heat from the plasma by radiating from the outer surfaces of the GCT, endplate, and choke, radially outward. This cooling concept is illustrated in Figure 2c. The heat flux to the cryo-magnets must be kept low so that they do not overheat. Therefore, some means of intercepting the radiation from the outside surfaces of the helicon hardware and transporting it upstream to be rejected to space, is required. To minimise radiated heat transfer to the thermal jacket, an annular layer of multi layer insulation (MLI) would be used, placed next to the thermal jacket. The proposed location of MLI is illustrated schematically in Figure 3. The radiative cooling strategy results in a relatively low-mass design, but may

lead to relatively high hardware temperatures. Due to the nature of radiation heat transfer, radiatively cooled designs can work very efficiently, but only at high temperatures. High emissivity black coatings would ideally be used on the outer surface of the GCT, endplate and choke to enhance radial heat transfer.

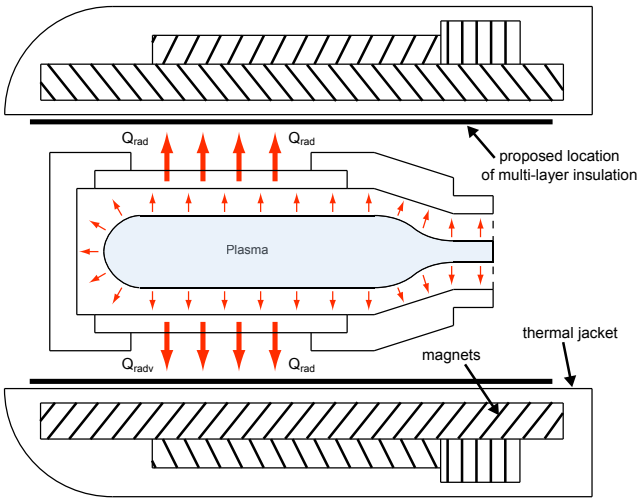

Figure 3: Location of multi-layer insulation (MLI) in the radiative cooling design to minimise heat transfer to the thermal jacket and magnets.

Radiated heat from the GCT, endplate and choke could be intercepted and efficiently transported axially upstream using an annular arrangement of heat pipes. The evaporators of the heat pipes would be located in an annular arrangement around the helicon section hardware, while their condensers would be incorporated into external thermal radiators. An alternative design could use an annulus of encapsulated annealed pyrolytic graphite (EAPG) to intercept radiated heat and transport it axially. Annealed pyrolytic graphite (APG) is a planar form of carbon with very high in-plane thermal conductivity. At 25 °C the in-plane thermal conductivity is $1950\,\mathrm{W \cdot m^{-1} \cdot K^{-1}}$ while perpendicular to the plane the thermal conductivity is $5.7\,\mathrm{W \cdot m^{-1} \cdot K^{-1}}$ [25]. However, APG has very low strength. For use in thermal management applications it is commonly embedded in a metal (e.g. aluminium, beryllium) or carbon composite casing. In this form the material is referred to as encapsulated annealed

pyrolytic graphite (EAPG). In order to reduce thermal contact resistance, intimate contact between the APG core and the encapsulation may be achieved, for example, by hot-isostatic-pressing the assembled composite structure [26].

2.4. Radial Cooling

The concept of radial cooling is to conduct the waste heat deposited on the inside of the GCT through a solid dielectric material out to the $4x$-distance, where it can be transported upstream using non-dielectric means. The rationale for pursuing this cooling design is that thermal gradients might be reduced by conducting the waste heat through the shortest possible path—directly radially outward. This conceptual cooling concept is illustrated in Figure 2d.

Implementation of the radial cooling strategy would most practically be achieved by encircling the GCT with a ceramic material that extends radially outward to the $4x$ distance. This component is hereafter referred to as the *ceramic layer*. This ceramic layer would ideally have high thermal conductivity. As discussed below, the GCT and ceramic layer could be integrated into a single ceramic component.

As for the radiative cooling design, an annular arrangement of heat pipes or an annulus of EAPG could be used to transport waste heat axially upstream. For the radial cooling design, however, these thermal management devices would be bonded to the outer surface of the ceramic layer, rather than intercepting radiated heat.

The main advantage of the radial cooling option is that the GCT will likely not heat up to temperatures as high as those reached in the radiation cooling strategy. The major disadvantage of the radial cooling design is that a large ceramic layer is required that would add greatly to the total mass of the helicon section.

2.5. Discussion of Conceptual Designs

Of the four different cooling system design options, axial, radiative and radial cooling designs are selected for further analysis. The fluid-assisted active

cooling design is not considered further in the current article. Actively pumped fluid cooling loops significantly complicate the design process and require extensive life testing programmes, typically leading to higher costs. Thermal and structural numerical analyses performed on these cooling designs are discussed in the following sections. The goal of these analyses is to determine which of the designs are feasible, and to determine which design leads to the lowest overall system mass at a given waste heat level.

Previous prototypes have utilised discrete metallic endplate, ceramic GCT, and metallic choke components. Stainless steel and aluminium alloys have previously been used for the endplate and choke. For the radiative cooling design, the endplate, GCT and choke could be manufactured as a single monolithic ceramic component. This would alleviate the problems with joints and mismatches in thermal expansion coefficients between the GCT and endplate and choke. This design would also eliminate the brazed interfaces between the GCT and the endplate and choke. A non-trivial difficulty associated with this design concept would be the difficulty in manufacture of such a large ceramic component. Additionally, the failure probability of a ceramic component increases with component size. This may be offset by having lower stresses. This strategy is assessed in the current analyses.

The geometry and hardware construction of the helicon sections in the previous VX-CR and VX-50 VASIMR® prototypes differed substantially from each other. Rather than being composed of a discrete endplate, GCT and choke, the VX-50 prototype used a long fused quartz GCT, which extended past the electromagnets in both the upstream and downstream directions [22]. The conceptual design studied has similar geometrical configuration to that of the VX-CR prototype [23], but has a GCT outer diameter approximately twice that of the VX-CR.

For the axial and radiative cooling designs the antenna is mounted with a small (3 mm) gap between the outer surface of the GCT and the inner surface of the antenna. Such a gap avoids the high interfacial thermal stresses that would occur if the antenna were directly bonded to a GCT of lower CTE. For

the radial cooling design the antenna is bonded between the outer surface of the GCT and the inner surface of the ceramic layer in order to provide an unbroken heat conduction path in the radial direction. In the axial and radiative designs the antenna is radiatively cooled, while for the radial cooling design heat is conducted away from the antenna into the ceramic layer.

Previous VASIMR® prototypes have utilised antennae constructed of hollow copper tubing brazed to thicker copper strips. De-ionised water is circulated through the hollow tubing to cool the antenna. Copper in the polished state has a very low emissivity of approximately 0.03 [27]. For the current application, the antenna would be coated with a dielectric thermal 'black' coating to enhance radiative heat rejection. The coating used must be transparent to the RF radiation.

3. Materials

An electrically-insulating material with low dielectric loss factor and high maximum operational temperature is required for the plasma discharge tube. Suitable materials for use for the plasma discharge tube, and the properties of these materials have been considered previously by the current authors [17, 28]. Four polycrystalline ceramics are evaluated for use as the GCT material in the current work: alumina, aluminium nitride, beryllia, and silicon nitride.

Fused quartz is widely used as a plasma discharge tube material in low-power devices. The maximum temperature at which fused quartz may operate, in order to allow for intermittent cooling to room temperatures, and to allow for a long lifetime (no formation of β-cristobalite), is ≈ 950 °C. Due to this limited maximum operation temperature, and its low thermal conductivity, fused quartz is not suitable for use at the high power levels considered in the current analyses.

Stainless steel 304 (UNS S30400) is assumed for the endplate and choke, and electronic-tough-pitch (ETP) copper (UNS C1100) is assumed for the helicon antenna material.

Temperature-dependent material property data, where available, have been

obtained from references [17] and [28], for use in the current thermal-structural analyses. Temperature-dependent properties are not available for some materials. Those material properties for which insufficient temperature-dependent data are available are assumed constant with respect to temperature. The assumed maximum operating temperature for each ceramic considered is given in Table 2.

Table 2: Assumed values of maximum allowable operating temperatre for thermal analyses.

Material	Temperature [°C]	Limiting Factor
Alumina	1400	Reduction in strength
Aluminium nitride	1400	Unknown flexural strength
Beryllia	1700	Grain growth
Silicon nitride	1200	Reduction in strength

It is assumed that the outer surfaces of the endplate, choke, GCT and antenna would be coated with a thermal black coating to maximise radiative heat rejection from these components. The assumed emissivity value is 0.88 (assumed to be independent of temperature), which is representative of commercially-available black thermal surface coatings [27].

4. Thermal-Structural Analyses

4.1. FEA Analysis Details

Thermal and structural numerical analyses were performed on the main helicon section hardware components of a conceptual VASIMR® prototype using ANSYS® Version 15.0 (ANSYS, Inc., Canonsburg, Pennsylvania, USA.), which calculates temperature and stress fields using a finite element method. The goal of these analyses was to determine the temperature and stress fields in the helicon section hardware components resulting from heat flux from the plasma and ohmic heating in the RF antenna.

Solid model 3D geometries were created using PTC Creo 2.0 (PTC, Needham, Massachusetts, USA) and imported into ANSYS DesignModeler 15.0. The solid model was meshed using SOLID87 and SOLID187 3D 10-node tetrahedral solid elements for thermal and structural analyses, respectively. Finer grid sizes were utilised at the interfaces between hardware components. Radiative and convective heat transfer modelling utilised SURF152 thermal surface effect elements. Governing equations of the models were solved using a sparse matrix direct solver for thermal analyses and pre-conditioned conjugate gradient solver for structural analyses.

The most promising conceptual cooling arrangements detailed in Section 2 were assessed: axial cooling, radiative cooling, radial cooling, and radiative cooling using a combined monolithic ceramic GCT, endplate, and choke. The all-ceramic radiative cooling design incorporates rounds in corner areas in order to avoid stress-raising geometry. For the axial and radiative cooling designs the GCT, endplate, choke and antenna were modelled. For the radial cooling design a ceramic layer surrounding the GCT and antenna was additionally modelled. One half of the hardware was modelled, utilising appropriate symmetry boundary conditions, to take advantage of the symmetry in the design, and thereby reduce solution times [29]. Once the temperature distribution was calculated, it was imported to a static-structural analysis as a degree-of-freedom constraint. The resultant stress and strain fields were then calculated.

4.2. Boundary Conditions

For the axial and radiative cooling designs radiation boundary conditions were applied to the outer surfaces of the GCT and antenna, with an environmental sink temperature of 20 °C.

The effective environmental temperature for radiative heat rejection from a spacecraft in orbit is a function of the radiator surface area, angle of inclination to the sun and earth, ratio of panel absorptivity to emissivity at the peak wavelengths of solar and planetary emissions, and the view factor to space [30, 31]. For a flat panel radiator with one active side with its plane at angle θ_s to the

incident solar irradiation, the absorbed solar heat flux is:

$$f_{\text{sol}} = \alpha_{\text{r}} S \sin\theta_{\text{s}} \tag{1}$$

Here α_{r} is the absorptivity of the radiator surface, and S is the solar constant (solar heat flux) at 1 astronomical unit (approximately $1370\,\text{W}\cdot\text{m}^{-2}$). Radiators of satellites in earth orbit also intercept solar radiation reflected from the earth's surface. If the radiator plane is at an angle θ_{p} to nadir, the absorbed heat flux due to reflected radiation from the earth's surface is given by:

$$f_{\text{ref}} = \tau_{\text{e}} A \left(\alpha_{\text{r}} S \sin\theta_{\text{p}}\right) \left(\frac{R_{\text{e}}}{R_{\text{e}} + H}\right)^2 \tag{2}$$

Here τ_{e} is the transmissivity of the earth's atmosphere, A is the albedo of the earth's surface, R_{e} is the radius of the earth, and H is the orbital altitude. In addition, the radiator will absorb a heat flux due to IR emission from the earth, given by:

$$f_{\text{IR}} = \tau_{\text{e}} \sigma \varepsilon_{\text{e}} T_{\text{e}}^4 \left(\alpha_{\text{r}} \sin\theta_{\text{p}}\right) \left(\frac{R_{\text{e}}}{R_{\text{e}} + H}\right)^2 \tag{3}$$

Here σ is the Stefan-Boltzmann constant, ε_{e} is the emissivity of earth, and T_{e} is the temperature of the earth's surface. Internally generated heat in a spacecraft that is rejected through a radiator surface leads to an increase in the radiator equilibrium temperature. The heat flux of internally generated heat rejected from the radiator surface is given by:

$$f_{\text{int}} = \frac{Q_{\text{int}}}{\zeta \varepsilon_{\text{r}} \eta A_{\text{r}}} \tag{4}$$

Q_{int} is rate of onboard heat generation (in watts), ζ is the view factor, η is the fin effectiveness of the radiator panel, A_{r} is the radiator surface area, and ε_{r} is the emissivity of the radiator surface. With the combined effects of direct solar irradiation, reflected radiation from the earth's surface, IR radiation from the earth's surface, and internal heat generation, the equilibrium temperature of a flat plate radiator may then be calculated as:

$$T_{\text{eq}} = \sqrt[4]{\frac{f_{\text{sol}} + f_{\text{ref}} + f_{\text{IR}} + f_{\text{int}}}{\zeta \sigma \varepsilon_{\text{r}}}} \tag{5}$$

These calculations are described in more detail by Juhasz [30].

By suitable selection of the radiator panel area (A_r), inclination angle, and surface coating, the effective radiation heat rejection temperature for spacecraft in Earth orbit may be adjusted to temperatures near 300 K. For the present analyses this effective heat rejection temperature is assumed to be 20 °C.

For the axial cooling design, the endplate and choke are constructed with internal cooling passages. 18 cooling passages are arranged azimuthally within these components. Water with the inclusion of corrosion inhibitors is assumed as the coolant. Convection cooling in these passages is modelled by applying a convection heat transfer boundary condition to the cooling passage surfaces. The applied heat transfer coefficient was $1000\,\mathrm{W \cdot m^{-2} \cdot K^{-1}}$. Evaluation of an average heat transfer coefficient for internal flow through such ducts may be achieved using a Nusselt number correlation. Correlations for internal flow in ducts of a variety of cross-sections have been compiled by Shah & London [32]. If required for future designs, enhancements in heat transfer coefficient for such cooling passages may be obtained by a number of means, including the use of axial or spiral grooves or fins within the passages.

The downstream end of the choke contains a reduction in radius. The helicon section hardware connects to the downstream ICRH section at this point. An insulated thermal boundary condition is applied at the downstream end of the choke.

The endplate and choke must be bonded to the GCT to form a gas-tight seal. As the temperatures at these locations can be above 300 °C, brazing rather than adhesive bonding is preferred. These joints are modelled as 'fully bonded' (i.e. fully coupled translation and rotational degrees of freedom) interfaces with zero interfacial thermal conduction resistance.

4.3. Structural Failure Modes

Temperature gradients in components cause differential expansion, which gives rise to thermal stresses. If these stresses are too high the material can fail. In general, the higher the thermal expansion coefficient, the higher will

be the thermal stresses generated due to the thermal strain. However, when contacting components are made of different materials the situation is more complex. The magnitude of the thermal stresses will depend on the thermal expansion coefficients of both materials.

The GCT must be strong enough to withstand thermal stresses that will develop due to differential expansion. The maximum normal stress failure criterion was used to assess the GCT and ceramic layer, while the Von Mises failure criterion was used to assess the endplate, choke, and antenna. Ceramics at moderate temperature fail in a brittle manner. The strength in tension of engineering ceramics is significantly lower than their strength in compression. The maximum-normal stress theory predicts material failure when one of the principal stresses in the material exceeds the strength of the material [33]:

$$\sigma_1 \geq \sigma_\mathrm{t} \qquad \text{or} \qquad \sigma_3 \leq -\sigma_\mathrm{c} \tag{6}$$

Here the principal stresses have been ordered so that $\sigma_1 \geq \sigma_2 \geq \sigma_3$. σ_t is the tensile strength and σ_c is the compressive strength.

4.4. Plasma Thermal Load

Knowledge of the thermal load caused by the plasma in current VASIMR® prototypes is essential to predict the thermal loads in higher power prototypes. The VASIMR® device is modelled in the present work at a total RF power input of 250 kW, which is higher than that of the current 200 kW VX-200 prototype.

Radiation from the plasma is in the hard UV spectrum and accounts for 23% of the heat load radially to the GCT walls [16]. The dominant source of heat load, accounting for the remaining 77% is from cross-field transport of charged particles impacting the tube [16]. High heating occurs close to the antenna, caused by fast ions that are accelerated by the antenna's electromagnetic field.

The VX-200 operates with a total of 200 kW of RF power, partitioned between the helicon plasma generation stage and ICRH stage. 35 kW of RF power is fed to the helicon section and the remaining 165 kW is fed to the ICRH

section [34, 13]. For the thermal design of higher power devices, this same proportion of total RF power between helicon and ICRH sections may be assumed.

The waste heat from the plasma has been previously investigated [35, 22, 16, 23]. Berisford *et al.* [35, 16] studied the University of Texas at Austin (UT) helicon plasma experiment, operated at 1.0 kW, measuring the heat flux incident upon the GCT and the radial heat flux to the vacuum chamber walls downstream of the GCT using an IR camera and bolometric probes. The heat fluxes incident upon the inner surface of the GCT of the VASIMR® VX-50 and VASIMR® VX-CR devices, operated at 16.2 kW and 1.4 kW respectively, were calculated by Mulcahy *et al.* [22] and de Faoite *et al.* [23], respectively, as a function of three controlled parameters (gas flowrate, current to electromagnets, and RF power input), using inverse methods.

The investigations by Mulcahy *et al.* [22] and de Faoite *et al.* [23] found that for a given magnetic field configuration and propellant flowrate, the peak heat flux and total heat load increased linearly with RF power input. These investigations also found that the spatial distribution of heat flux on the tube was not significantly affected by RF power input. These results are used in the current work to estimate the waste heat load at higher RF power inputs.

Using this linear correlation between peak heat flux and RF power, the quantitative relation between peak heat flux occurring on the GCT inner surface and RF power input may be analysed for each of the experiments of Berisford *et al.*, Mulcahy *et al.* and de Faoite *et al.* For example, an experiment by Berisford *et al.* [16] on the UT helicon plasma experiment found a peak heat flux of $6\,\mathrm{kW \cdot m^{-2}}$ at a power input of 970 W. A zero-intercept linear regression fit was applied individually to the datasets of peak heat flux vs. input power, of Berisford *et al.*, Mulcahy *et al.* and de Faoite *et al.*, and then to the combined dataset. This linear fit implies a relation of the type:

$$q_\mathrm{p} = \lambda P_\mathrm{RF} \tag{7}$$

where q_p is the peak heat flux, P_RF is the applied RF power input, and λ is a constant. The experiment of Berisford *et al.* found $q_\mathrm{p} = \left(6.19\,\mathrm{m^{-2}}\right) P_\mathrm{RF}$;

the 9 experiments of Mulcahy *et al.* found $q_{\mathrm{p}} = \left(7.26\ \mathrm{m}^{-2}\right) P_{\mathrm{RF}}$, and the 18 experiments of de Faoite *et al.* found $q_{\mathrm{p}} = \left(8.58\ \mathrm{m}^{-2}\right) P_{\mathrm{RF}}$ respectively. These three figures are in reasonable agreement. The three datasets were combined into a single dataset and a zero-intercept straight-line fit was calculated for the combined data, yielding the function: $q_{\mathrm{p}} = \left(7.293\ \mathrm{m}^{-2}\right) P_{\mathrm{RF}}$. This is the value that is assumed in this work for estimating the heat flux for the higher power VASIMR® devices.

The VX-50 and VX-CR had approximately the same diameter. The VX-200 and other future VASIMR® devices will have larger diameter GCTs. Making the assumption that the thermal power transferred from the plasma to the GCT per unit axial length is not dependent upon the diameter of the GCT, we can use the following equation to calculate the heat flux for a different diameter GCT:

$$q\left(z\right) = \frac{r_1}{r_2}\left(\lambda P_{\mathrm{RF}} \bar{F}\left(z\right)\right) \tag{8}$$

Here r_1 is the inner radius of the VX-50 prototype and r_2 is the inner radius of the high-power conceptual prototype. The function $\bar{F}$ is the averaged normalised axial heat flux profile (given by Eq. (10)), and z is the axial coordinate. Scaling from the inner radius for the VX-CR and VX-50 up to the inner radius for a conceptual high power VASIMR® prototype results in a scaling of the heat flux by 0.594. This procedure was used by Mulcahy [36]. Implementing this spatial-scaling, the helicon section power and peak heat flux on the GCT inner surface for a considered power level of 250 kW are shown in Table 3.

The investigations by Mulcahy *et al.* and de Faoite *et al.* found both axial and azimuthal variation in heat flux to the GCT. The axial variation in heat flux was found to be more significant than the azimuthal variation, and so for the current analyses the azimuthal variation is neglected. Berisford *et al.* measured a peak in heat flux at the downstream helicon antenna strap [16]. Mulcahy *et al.* reported localised heating downstream of the helicon antenna of the VX-50 [22], while de Faoite *et al.* found that for the VX-CR prototype the location of peak heat flux was centered relative to the antenna [23].

A peak-normalisation fitting porcedure was used to calculate an azimuthally-averaged axial heat flux profile based on the combined data from the UT helicon experiment, and VX-50 and VX-CR VASIMR® prototypes. A normalised axial heat flux profile was created by dividing the heat flux axial distribution by the peak heat flux that occurs:

$$F(z) = \frac{q(z)}{q_{\mathrm{p}}} \tag{9}$$

When averaged over all experiments, the average of the normalised heat fluxes are denoted $\bar{F}(z)$. That is:

$$\bar{F}(z) = \frac{1}{N_{\mathrm{e}}} \sum_{n=1}^{N_{\mathrm{e}}} F_n(z) \tag{10}$$

The VX-CR, VX-50 and UT helicon plasma experiment all have different geometries, including different tube lengths and antenna lengths. In order to relate the heat flux profiles calculated by for each device, these heat flux profiles were referenced using the downstream antenna strap as a common reference point. The peak-normalised axial heat flux profiles from the experiments of Berisford *et al.*, Mulcahy *et al.* and de Faoite *et al.* relative to the downstream antenna strap are plotted in Figure 4. The axial heat flux profiles of Berisford *et al.* and de Faoite *et al.* coincide closely and in both cases a large heat flux occurs at the centre of the GCT (where the cooling requirements are most severe). A curve fit (Figure 4) was performed on the data of these two experiments to generate an axial heat flux profile for use in the present thermal-structural analyses. The heat flux at a given power level is calculated by multiplying this peak-normalised axial heat flux profile by the RF power and the scaling factor λ:

$$q(z) = \lambda P_{\mathrm{RF}} \bar{F}(F(z)) \tag{11}$$

The axial heat flux profiles scaled to the considered power level of 250 kW is plotted in Figure 5.

Analysis of the VX-CR helicon section found that the temporal variation of plasma waste heat flux was slight [23]. The heat load is therefore considered steady in the current analysis.

Table 3: Power to helicon section and waste heat for 250 kW RF power input.

RF Power Input [kW]	RF Power to Helicon Section [kW]	Thermal Power to GCT [kW]	Peak GCT Heat Flux $[\mathrm{kW \cdot m^{-2}}]$	Thermal Power to Helicon Antenna [kW]
250	43.750	17.28125	189.447	0.875

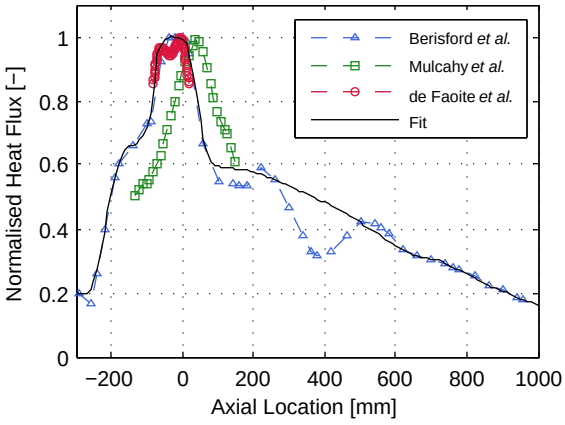

Figure 4: Heat flux axial profiles measured by Berisford *et al.* [16], Mulcahy *et al.* [22] and de Faoite *et al.* [23]. The axial position is relative to the antenna centre for each experiment.

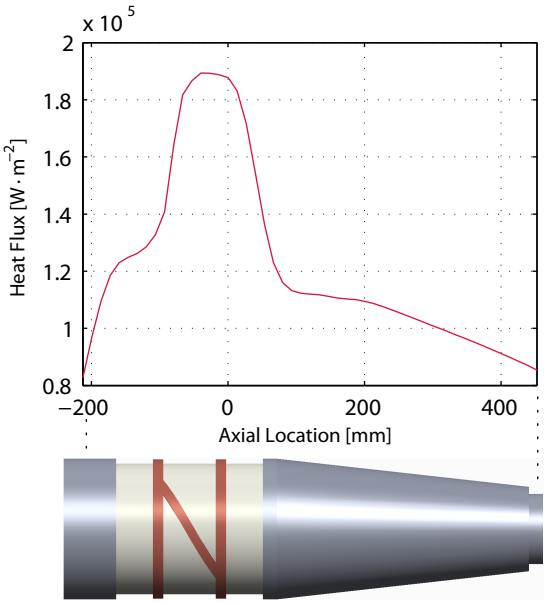

Figure 5: Assumed axisymmetric heat flux profile from plasma to inner surfaces of GCT, endplate and choke as a function of axial position. An image of the helicon hardware assembly is shown below the plot for ease of reference.

4.5. Antenna Ohmic Heating

Heating of the helicon antenna occurs due to Joule heating. Radio frequency electrical current flows in a thin layer at the outer surface of a conductor, a tendency referred to as the 'skin effect'. Berisford *et al.* [35, 16] measured the power loss in a helicon antenna as being 2% of the antenna input RF power, and note that this figure is slightly higher than the power loss calculated due to Joule heating when the current is assumed to penetrate to the skin depth [37]. This value from Berisford *et al.* is assumed in this work. Assuming 17.5% of input RF is partitioned to the helicon section, 0.35% of the total RF power is converted to heat in the helicon antenna. The antenna heat load for the modelled RF power input of 250 kW is given in Table 3.

4.6. Modelling of Interfaces

Hamlyn-Harris *et al.* modelled an RF vacuum window that contained interfaces between beryllia and titanium components [38]. They assessed the effect of modelling the braze material on the calculated stress results. They first modelled the joint between the metal and ceramic as a rigid bond with no braze material as a benchmark, and then modelled the joint including the braze material. They studied braze thicknesses between 50 µm and 150 µm. They found that when modelling the braze there was a slight reduction in peak stress near the braze, but that the effect on the stress field overall was insignificant. The braze material will therefore not be modelled in this work. Instead, the interface is modelled numerically as a perfectly bonded joint.

5. Results and Discussion

5.1. Thermal Analysis Results

The steady-state temperature distributions for a silicon nitride GCT at the 250 kW power input level for each of the designs are shown in Figure 6. The temperature distributions for the other GCT materials are similar in distribution,

but vary in magnitude. The calculated maximum GCT steady-state temperatures for the axial, radiative, radial, and all-ceramic radiative cooling designs are given in Table 4. As expected, the highest temperatures occur on the inner surface of the GCT. The axial centre of the GCT reaches a higher temperature than the ends, and therefore expands more than the tube ends, with obvious implications for thermal stress generation.

For axial cooling, the silicon nitride GCT reaches the greatest fraction of its absolute maximum allowable operation temperature. Despite the higher room temperature thermal conductivity of beryllia, the thermal conductivity of aluminium nitride decreases more slowly with increasing temperature than beryllia does [17, 28]. The aluminium nitride GCT therefore reaches a lower peak temperature than the beryllia GCT.

For the axial and radiative cooling designs the central portion of the GCT heats up the most, as this is the location of peak heat flux. Locally high temperatures occur in the downstream end of the choke. As the end of the choke will interface to the downstream hardware its outer surface is not free to radiate heat away, leading to a high temperature. For the radial cooling design the location of peak temperature is in the choke, which heats up to a comparable temperature to the choke in the radiative cooling design as it rejects heat solely by radiation.

The axial cooling design results in very low temperatures in the endplate and choke. However, the GCT still heats up significantly. The maximum temperatures in the GCT for the axial and radiative designs with an alumina GCT are 1345 °C and 1344 °C respectively. That is, axial cooling of the endplate and choke results in almost no reduction in peak GCT temperature. For a silicon nitride GCT axial cooling results in only a 4 °C reduction in peak GCT temperature. These reductions in temperature are small due to the low thermal conductivity of alumina and silicon nitride. For aluminium nitride and beryllia the reductions arising from use of axial cooling are 46 °C and 29 °C, respectively. It may be concluded that axial cooling is effective in reducing GCT peak temperature, but only when the thermal conductivity of the GCT is high. For lower

Table 4: GCT, endplate and choke maximum steady-state temperature for the axial, radial, radiative and all-ceramic radiative cooling designs. The all-ceramic cooling design has a combined GCT, endplate, and choke. The maximum temperatures of this combined component are given in the GCT category.

Cooling Strategy	Material	GCT Max. Temperature [°C]	Endplate Max. Temperature [°C]	Choke Max. Temperature [°C]
Axial	Al_2O_3	1345.4	389.3	505.6
	AlN	1062.9	464.9	567.9
	BeO	1118.6	444.8	547.3
	Si_3N_4	1206.6	415.6	531.0
Radial	Al_2O_3	806.3	805.2	1028.1
	AlN	253.4	692.9	1027.9
	BeO	206.2	681.7	1027.9
	Si_3N_4	717.5	790.2	1028.1
Radiative	Al_2O_3	1344.3	843.7	1026.1
	AlN	1108.4	849.2	1026.1
	BeO	1147.4	847.4	1026.1
	Si_3N_4	1210.4	845.0	1026.1
All-Ceramic	Al_2O_3	1345.0	-	-
	AlN	1116.2	-	-
	BeO	1152.4	-	-
	Si_3N_4	1212.3	-	-

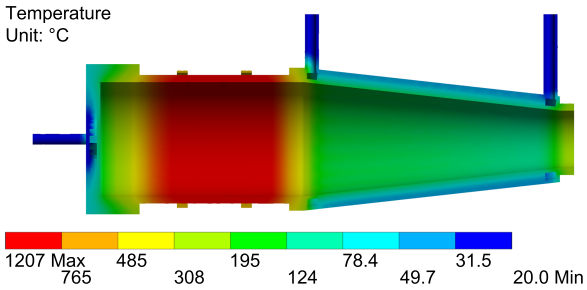

(a) Axial cooling.

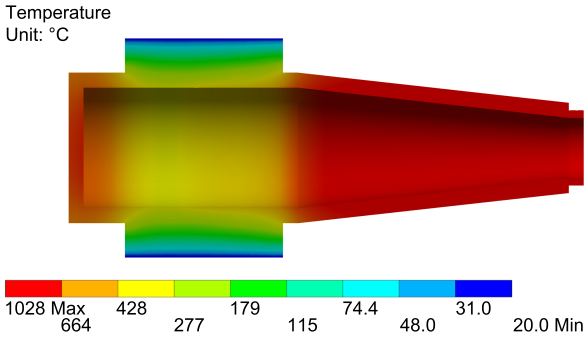

(b) Radiative cooling.

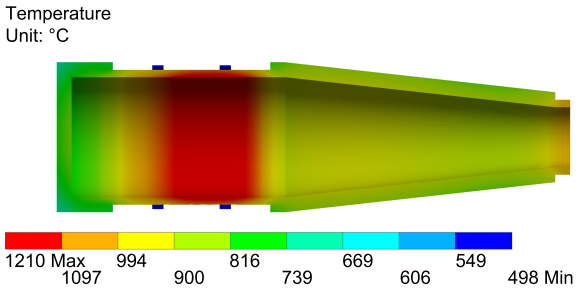

(c) Radial cooling.

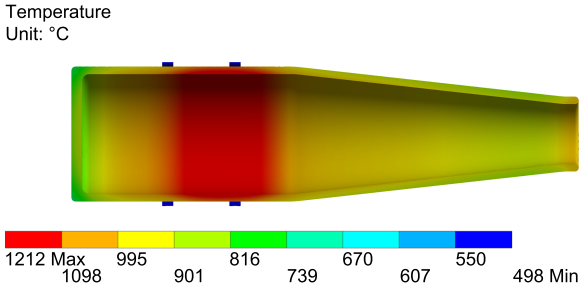

(d) Radiative cooling, all-ceramic design.

Figure 6: Temperature distribution in the helicon section hardware with 250 kW RF power input and with a silicon nitride GCT.

thermal conductivity materials such as alumina and silicon nitride, the added complexity of axial cooling does not result in any significant reduction in GCT temperature.

Radial cooling results in the lowest GCT temperatures. Similar to axial cooling, the goal of radial cooling is to conduct heat away from the GCT. However, with radial cooling the length over which heat must be conducted is shorter than that in the axial cooling design, resulting in lower temperature resistance. In the current design, the endplate and choke still heat up significantly as these dissipate heat by radiative heat transfer. It has been assumed that outer radial surface of the ceramic layer can be cooled to room temperature. Achievement of this idealised thermal boundary condition requires careful design of a heat transport mechanism—such as an array of heat pipes or EAPG—to external thermal radiators.

Cooling by radiative heat transfer becomes more effective at higher temperatures. As a result, maximum operating temperature plays a significant role in the selection of a material for this application, if radiative heat transfer is intended to be the main cooling mechanism.

5.2. Structural Analysis Results

The Von Mises stress in the metallic components, and the maximum and minimum principal stresses in the ceramic components for the axial, radial, radiative, and all-ceramic cooling designs are shown in Figures 7–8 for a silicon nitride GCT at the 250 kW power input level. The stress distributions for the other GCT materials are similar in distribution, but vary in magnitude. The calculated maximum values of Von Mises stress in the metallic components, and the maximum values of maximum principal stress and minimum principal stresses in the ceramic components, are given in Table 5.

For the axial, radiative, and radial cooling designs the location of peak Von Mises stress in the metallic components occurs at the interfaces between the endplate, GCT, and choke. The stainless steel endplate and choke have a significantly higher CTE than any of the four ceramic GCT materials consid-

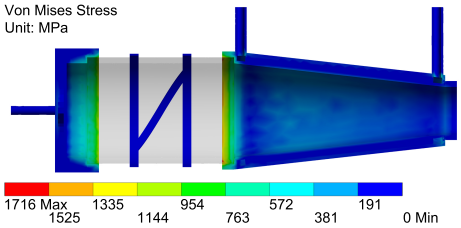

(a) Von Mises stress for the metallic components of the axial cooling design.

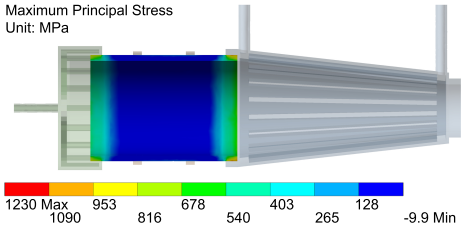

(b) Maximum principal stress for the GCT of the axial cooling design.

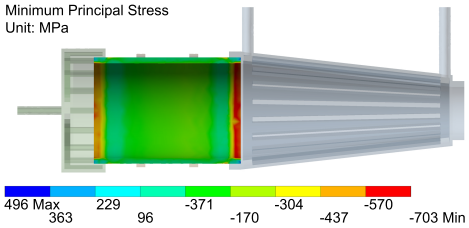

(c) Minimum principal stress for the GCT of the axial cooling design.

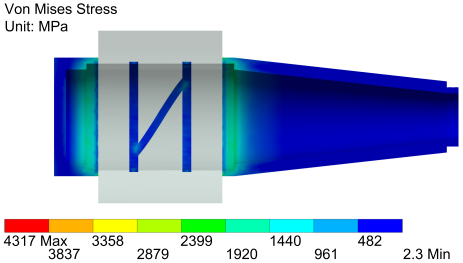

(d) Von Mises stress for the metallic components of the radial cooling design.

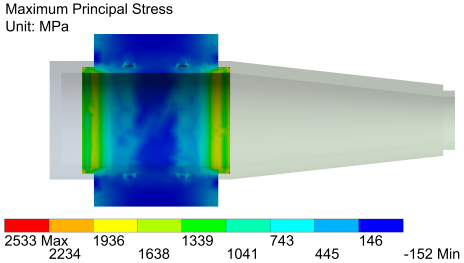

(e) Maximum principal stress for the GCT of the radial cooling design.

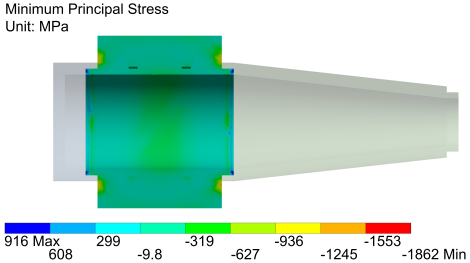

(f) Minimum principal stress for the GCT of the radial cooling design.

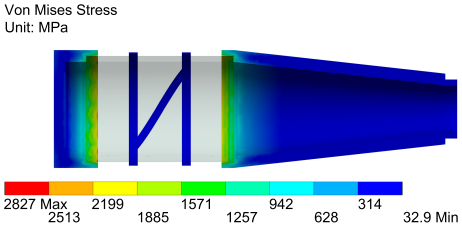

(g) Von Mises stress for the metallic components of the radiative cooling design.

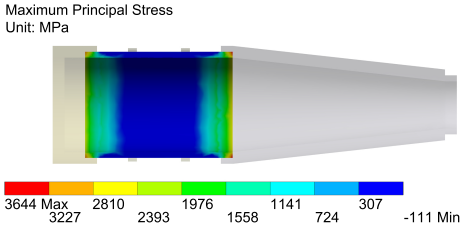

(h) Maximum principal stress for the GCT of the radiative cooling design.

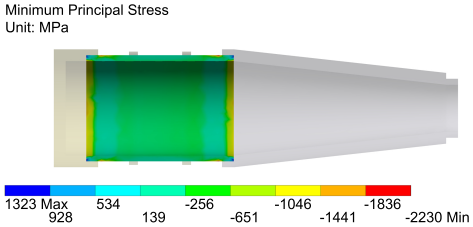

(i) Minimum principal stress for the GCT of the radiative cooling design.

Figure 7: Von Mises, maximum principal, and minimum principal stresses for a silicon nitride GCT, stainless steel 304 endplate and choke, and copper antenna, for the axial, radial, and radiative cooling designs.

Table 5: Structural analyses results: maximum values of Von-Mises stress (σ_{vm}) in the metallic components; maximum values of maximum principal stress (σ_1) and minimum principal stresses (σ_3) in the ceramic components.

Cooling Strategy	Material	σ_{vm} [MPa]	σ_1 [MPa]	σ_3 [MPa]
Axial	Al_2O_3	1159.0	998.4	−992.5
	AlN	1656.2	1218.9	−769.7
	BeO	1283.0	922.7	−544.5
	Si_3N_4	1716.1	1228.4	−703.2
Radial	Al_2O_3	3506.8	2056.4	−1539.0
	AlN	2144.6	468.9	−2853.9
	BeO	1841.6	1285.6	−270.6
	Si_3N_4	4316.6	2532.7	−635.5
Radiative	Al_2O_3	1994.7	2913.3	−1549.0
	AlN	2454.2	2950.1	−1911.0
	BeO	1904.4	2443.2	−1528.2
	Si_3N_4	2827.3	3644.5	−2230.0
All-Ceramic	Al_2O_3	-	672.6	−711.7
	AlN	-	84.7	−89.6
	BeO	-	248.9	−263.6
	Si_3N_4	-	131.5	−139.0

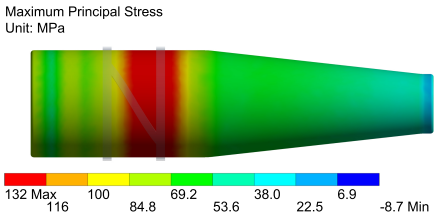

(a) Maximum principal stress for the GCT of the all-ceramic radiative cooling design.

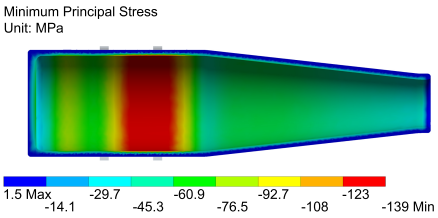

(b) Minimum principal stress for the GCT of the all-ceramic radiative cooling design.

Figure 8: Von Mises, maximum principal, and minimum principal stresses for a silicon nitride GCT, stainless steel 304 endplate and choke, and copper antenna, for the all-ceramic radiative cooling design.

ered. When heated, the endplate and choke tend to expand more than the GCT, resulting in the ends of the GCT being pulled outward. For the axial, radiative, and radial cooling designs the Von Mises stress in the root of the interfaces between the endplate, GCT, and choke is above the tensile yield strength of stainless steel 304. This would result in local yielding or failure of the brazed joint between the GCT and the endplate and choke. For these designs the highest value of GCT maximum principal stress occurs on the outer surface of the GCT at the interface to the choke. For the radial cooling design additional areas of high maximum principal stress occur on the inner surface of the tube close to the interfaces to the endplate and choke. These are termed 'pinch' stresses and are caused by the difference in CTE between the joining materials.

The highest maximum principal stresses in the GCT occur with the radiative cooling design. For this design the endplate and choke heat up to higher temperatures than occurs in the axial or radial cooling designs. This results in a greater tendancy for expansion of these components, inducing stresses in the ends of the GCT.

This analysis predicts that failure will occur in the endplate and choke or interfaces between the endplate, GCT, and choke, for the axial, radiative and radial cooling designs. This is due to the large difference in CTE between the

metallic endplate and choke and the ceramic GCT. Several potential solutions exist to this problem, described below.

Compliant Layers A compliant (low stiffness) material may be used in the interface between the GCT and the endplate and choke. Such a layer accommodates the differential strains between the components without generating excessively high stresses.

MMC Endplate and Choke The endplate and choke may be constructed from a metal-matrix composite. Metal-matrix composites can contain a ceramic or graphitic phase that results in a significant reduction in CTE. The CTE of MMCs are tailorable to an application by controlling the quantity and morphology of reinforcement material added [39]. Use of such a material would result in reduced CTE mis-match, and therefore reduced stresses.

All-Ceramic Design Construction of the endplate, GCT, and choke as a single monolithic ceramic component would avoid problems with mis-match in CTE, and therefore result in reduced stresses. Use of such a design would also avoid the requirement for the careful design of brazed joints between the GCT and the endplate and choke.

Modelling of an all-ceramic design utilising a combined GCT, endplate, and choke has been conducted for alumina, aluminium nitride, beryllia, and silicon nitride materials. Maximum and minimum principal stresses for this design for silicon nitride are shown in Figures 8a–8b. For this design the Von Mises stresses in the only metallic component—the antenna—are not shown as they are very low. The maximum and minimum principal stresses in the ceramic component for this design are significantly lower than those occurring in the other designs. The stresses in the alumina component are highest, due to alumina's combination of lower thermal conductivity and higher CTE. The lowest stresses occur with the use of aluminium nitride. For this design aluminium nitride has sufficient strength to perform adequately at the modelled heat load.

6. Discussion and Conclusions

Thermal and structural analyses have been performed on the GCT of a high-power electric propulsion plasma rocket engine. The plasma causes a significant thermal load on the GCT, endplate, and choke, caused by cross-field particle diffusion and hard UV radiation.

Dielectric heating of the GCT has not been considered in the current analyses. The heat flux values calculated by Berisford *et al.* [16], Mulcahy *et al.* [36] and de Faoite *et al.* [23] were for a fused quartz GCT, which has a low dielectric loss tangent, so dielectric heating would be low. The dielectric loss tangent tends to increase at higher temperatures, so a ceramic operating at high temperature would experience increased dielectric heating.

The stress in the helicon section is significantly affected by the interfaces between the endplate and tube, and choke and tube. Metal-matrix composites may be investigated for use for the endplate and choke. The CTE of MMCs is tailorable, and could be designed to match that of a ceramic GCT material. This would reduce problems with CTE mis-match.

The assessment of the susceptibility of the design to fatigue failure, caused by repeated on-off cycles, remains to be assessed. Additionally, analysis of the effects of the plasma on the plasma-facing surface materials remains to be thoroughly investigated.

A potential thermal management strategy for the helicon section of a potential high-power VASIMR® electric propulsion thruster has been analysed. With a combined endplate, GCT and choke fabricated from aluminium nitride, the design may operate successfully up to 250 kW of RF power input. Heat rejection from this component occurs primarily by radiation heat transfer in the radial direction. The adequacy of the ceramic component is based on the maximum normal failure criterion. The key difficulty in this design is in minimising the stresses in the ceramic GCT.

A design utilising a combined GCT, endplate, and choke was found to result in significantly lower stresses than one with separate endplate, GCT and choke.

Of the four polycrystalline materials assessed, alumina was found to result in the highest stresses, due to its combination of high CTE and moderate thermal conductivity. Aluminium nitride was found to result in the lowest temperatures and stresses.

This cooling strategy is applicable not only to the specifically-considered prototype, but also broadly applicable to future VASIMR® flight prototypes.

References

[1] F. R. Chang, J. L. Fisher, A supersonic gas target for a bundle divertor plasma, Nuclear Fusion 22 (1982) 1003. doi:10.1088/0029-5515/22/8/001.

[2] F. R. Chang-Diaz, The VASIMR rocket, Scientific American 283 (5) (2000) 90–97.

[3] F. R. Chang-Díaz, J. P. Squire, A. V. Ilin, G. E. McCaskill, T. X. Nguyen, D. S. Winter, A. J. Petro, G. W. Goebel, L. D. Cassady, K. A. Stokke, C. E. Dexter, T. P. Graves, L. Amador Jr., J. A. George, M. D. Carter, F. W. Baity Jr., G. C. Barber, R. H. Goulding, D. O. Sparks, S. W. Schwenterly, R. D. Bengston, B. N. Breizman, V. T. Jacobson, A. V. Arefiev, R. Z. Sagdeev, K. Karavasilis, S. V. Novakovski, A. A. Chan, T. W. Glover, The development of the VASIMR engine, in: International Conference on Electromagnetics in Advanced Applications, Torino, Italy, 1999.

[4] F. R. Chang-Díaz, J. P. Squire, R. D. Bengston, B. N. Breizman, F. W. Baity, M. D. Carter, The physics and engineering of the VASIMR engine, in: 36$^{\text{th}}$ AIAA/ASME/SAE/ASEE Joint Propulsion Conference, Huntsville, Alabama, 2000, AIAA 2000-3756.

[5] F. F. Chen, Plasma ionization by helicon waves, Plasma Physics and Controlled Fusion 33 (4) (1991) 339–364. doi:10.1088/0741-3335/33/4/006.

[6] J. Squire, F. Chang-Diaz, T. Glover, V. Jacobson, G. McCaskill, D. Winter, F. Baity, M. Carter, R. Goulding, High power light gas helicon plasma

source for VASIMR, Thin Solid Films 506 (2006) 579–582. doi:10.1016/j.tsf.2005.08.061.

[7] E. A. Bering III, F. R. Chang-Díaz, J. P. Squire, V. Jacobson, L. D. Cassady, M. Brukardt, High power ion cyclotron heating in the VASIMR engine, in: 45th AIAA Aerospace Sciences Meeting and Exhibit, no. AIAA-2007-586, Reno, Nevada, U.S.A., 2007. doi:10.2514/6.2007-586.

[8] E. A. Bering, F. R. Chang-Díaz, J. P. Squire, M. Brukardt, T. W. Glover, R. D. Bengtson, V. T. Jacobson, G. E. McCaskill, L. Cassady, Electromagnetic ion cyclotron resonance heating in the VASIMR, Advances in Space Research 42 (2008) 192–205. doi:10.1016/j.asr.2007.09.034.

[9] A. V. Arefiev, B. N. Breizman, Magnetohydrodynamic scenario of plasma detachment in a magnetic nozzle, Physics of Plasmas 12 (043504). doi:10.1063/1.1875632.

[10] A. V. Ilin, F. R. Chang-Díaz, J. P. Squire, B. N. Breizman, M. D. Carter, Particle simulations of plasma heating in VASIMR, in: 36th AIAA/ASME/SAE/ASEE Joint Propulsion Conference, no. AIAA 2000-3753, Huntsville, Alabama, U.S.A., 2000. doi:10.2514/6.2000-3753.

[11] G. B. Ribeiro, F. A. Braz Filho, L. N. F. Guimarães, Thermodynamic analysis and optimization of a Closed Regenerative Brayton Cycle for nuclear space power systems, Applied Thermal Engineering 90 (2015) 250–257. doi:10.1016/j.applthermaleng.2015.06.093.

[12] E. A. Bering, III, B. W. Longmier, J. P. Squire, T. W. Glover, L. D. Cassady, A. V. Ilin, M. D. Carter, C. S. Olsen, G. E. McCaskill, F. R. Chang Díaz, Performance measurements and technology demonstration of the VASIMR® vx-200, in: AIAA Space 2010 Conference and Exposition, no. AIAA-2010-8673, Anaheim, California, U.S.A., 2010. doi:10.2514/6.2010-8669.

[13] B. W. Longmier, J. P. Squire, L. D. Cassady, M. G. Ballenger, M. D. Carter, C. Olsen, A. V. Ilin, T. W. Glover, G. E. McCaskill, F. R. Chang Díaz, E. A. Bering III, J. Del Valle, VASIMR® VX-200 performance measurements and helicon throttle tables using argon and krypton, in: 32nd International Electric Propulsion Conference, no. IEPC-2011-156, Wiesbaden, Germany, 2011.

[14] J. A. Castro Nieto, J. Del Valle, C. Martínez, A. Rivera, J. Oguilve, C. S. Olsen, M. Giambusso, M. D. Carter, J. P. Squire, F. R. Chang Díaz, VASIMR® VX-CR experiment: Status, diagnostics and plasma plume characterization, in: 33rd International Electric Propulsion Conference, Washington, D.C., USA, 2013.

[15] O. Batishchev, K. Molvig, F. R. Chang-Diaz, J. P. Squire, Study of gas burn-out regime in the VASIMR helicon plasma source, in: 30th EPS Conference on Controlled Fusion and Plasma Physics, St. Petersburg, Russia, 2003.

[16] D. F. Berisford, R. D. Bengtson, L. L. Raja, Power balance and wall erosion measurements in a helicon plasma, Physics of Plasmas 17 (033503). doi:10.1063/1.3304184.

[17] D. de Faoite, D. J. Browne, F. R. Chang-Díaz, K. T. Stanton, A review of the processing, composition, and temperature-dependent mechanical and thermal properties of dielectric technical ceramics, Journal of Materials Science 47 (10) (2012) 4211–4235. doi:10.1007/s10853-011-6140-1.

[18] D. D. Blackwell, F. F. Chen, Two-dimensional imaging of a helicon discharge, Plasma Sources Science & Technology 6 (4) (1997) 569–576. doi:10.1088/0963-0252/6/4/015.

[19] T. Tanikawa, S. Shinohara, Plasma performance in very large helicon device, Thin Solid Films 506 (2006) 559–563. doi:10.1016/j.tsf.2005.08.053.

[20] K. Toki, , S. Shinohara, T. Tanikawa, K. P. Shamrai, Small helicon plasma source for electric propulsion, Thin Solid Films 506 (2006) 597–600. doi:10.1016/j.tsf.2005.08.039.

[21] H. Chen, E. Kallos, P. Muggli, T. C. Katsouleas, M. A. Gundersen, A high-density hydrogen-based capillary plasma source for particle-beam-driven Wakefield accelerator applications, IEEE Transactions on Plasma Science 37 (3) (2009) 456–462. doi:10.1109/TPS.2008.2011799.

[22] J. M. Mulcahy, D. J. Browne, K. T. Stanton, F. R. Chang-Diaz, L. D. Cassady, D. F. Berisford, R. D. Bengtson, Heat flux estimation of a plasma rocket helicon source by solution of the inverse heat conduction problem, International Journal of Heat and Mass Transfer 52 (9-10) (2009) 2343–2357. doi:10.1016/j.ijheatmasstransfer.2008.10.031.

[23] D. de Faoite, D. Browne, J. I. Del Valle Gamboa, K. Stanton, Inverse estimate of heat flux on a plasma discharge tube to steady-state conditions using thermocouple data and a radiation boundary condition, International Journal of Heat and Mass Transfer 77 (2014) 564–576. doi:10.1016/j.ijheatmasstransfer.2014.04.069.

[24] R. J. Sedwick, M. F. DeMaio, Superconducting helicon thrusters, in: 48$^{\text{th}}$ AIAA Aerospace Sciences Meeting Including the New Horizons Forum and Aerospace Exposition, 2010. doi:10.2514/6.2010-621.

[25] C. Y. Ho, R. W. Powell, P. E. Liley, Thermal conductivity of the elements: A comprehensive review, Journal of Physical and Chemical Reference Data 3 (Supplement No. 1) (1974) I–1–I–796.

[26] S. Kugler, Aluminum encapsulated APG high conductivity thermal doubler, in: 49$^{\text{th}}$ AIAA/ASME/ASCE/AHS/ASC Structures, Structural Dynamics, and Materials Conference, no. AIAA 2008-1861, Schaumburg, Illinois, USA, 2008.

[27] D. G. Gilmore (Ed.), Spacecraft Thermal Control Handbook Volume I: Fundamental Technologies, The Aerospace Press, 2002.

[28] D. de Faoite, D. J. Browne, K. T. Stanton, Regression analysis of temperature-dependent mechanical and thermal properties of dielectric technical ceramics, Journal of Materials Science 48 (1) (2013) 451–461. doi:10.1007/s10853-012-6759-6.

[29] Y. Nakasone, S. Yoshimoto, T. A. Stolarski, Engineering Analysis with ANSYS Software, Elsevier Butterworth-Heinemann, 2006.

[30] A. J. Juhasz, An analysis and procedure for determining space environmental sink temperatures with selected computational results, Tech. Rep. NASA/TM-2001-210063, Glenn Research Center, National Aeronautics and Space Administration (2001).

[31] A. J. Juhasz, Radiation in space and its control of equilibrium temperatures in the solar system, in: 34^{th} International Conference on Environmental Systems (ICES), Colorado Springs, USA, 2004.

[32] R. K. Shah, A. L. London, Laminar Flow Forced Convection in Ducts: A Source Book for Compact Heat Exchanger Analytical Data, Academic Press, New York, 1978.

[33] J. K. Budynas, R. G. Nisbett, Shigley's Mechanical Engineering Design, 8th Edition, McGraw-Hill, 2008.

[34] E. A. Bering, III, B. W. Longmier, M. Ballenger, C. S. Olsen, J. P. Squire, F. R. Chang Díaz, Performance studies of the VASIMR®, in: 49^{th} AIAA Aerospace Sciences Meeting and Exhibit, no. AIAA-2011-1071, Orlando, Florida, USA, 2011. doi:10.2514/6.2011-1071.

[35] D. F. Berisford, R. D. Bengtson, L. L. Raja, L. D. Cassady, W. J. Chancery, Heat flow diagnostics for helicon plasmas, Review of Scientific Instruments 79 (10F515). doi:10.1063/1.2955710.

[36] J. M. Mulcahy, Thermal characterisation of a plasma rocket and development of a thermal management system, Ph.D. thesis, University College Dublin (2010).

[37] C. Charles, R. W. Boswell, M. A. Lieberman, Energy balance in a low pressure capacitive discharge driven by a double saddle antenna, Physics of Plasmas 10 (2003) 891–899. doi:10.1063/1.1555058.

[38] C. Hamlyn-Harris, A. Borthwick, J. Fanthome, C. Waldon, M. Nightingale, N. Richardson, Engineering design of an RF vacuum window for the ITER ICRH antenna, Fusion Engineering and Design 84 (2-6) (2009) 887–894. doi:10.1016/j.fusengdes.2008.12.124.

[39] K. U. Kainer, Metal Matrix Composites: Custom-Made Materials for Automotive and Aerospace Engineering, Wiley, 2006. doi:10.1002/3527608117.